Transient and steady state creep response of ice I and magnesium sulfate hydrate eutectic aggregates

Christine McCarthy,[1,2] Reid F. Cooper,[1] David L. Goldsby,[1] William B. Durham,[3] and Stephen H. Kirby[4]

[1]   Using uniaxial compression creep experiments, we characterized the transient and steady state deformation behaviors of eutectic aggregates of system ice I and $MgSO_4 \cdot 11H_2O$ (MS11; meridianiite), which has significance because of its likely presence on moons of the outer solar system. Synthetic samples of eutectic liquid bulk composition, which produce eutectic colonies containing 0.35–0.50 volume fraction MS11, were tested as functions of colony size and lamellar spacing, temperature (230–250 K), and confining pressure (0.1 and 50 MPa) to strains ≤ 0.2. Up to a differential stress of 6 MPa, the ice I-MS11 aggregates display an order of magnitude higher effective viscosity and higher stress sensitivity than do aggregates of pure polycrystalline ice at the same conditions. The creep data and associated microstructural observations demonstrate, however, that the aggregates are additionally more brittle than pure ice, approaching rate-independent plasticity that includes rupture of the hydrate phase at 6–8 MPa, depending on the scale of the microstructure. Microstructures of deformed samples reveal forms of semibrittle flow in which the hydrate phase fractures while the ice phase deforms plastically. Semibrittle flow in the icy shell of a planetary body would truncate the lithospheric strength envelope and thereby decrease the depth to the brittle-ductile transition by 55% and reduce the failure limit for compressional surface features from 10 to ~6 MPa. A constitutive equation that includes eutectic colony boundary sliding and intracolony flow is used to describe the steady state rheology of the eutectic aggregates.

1.   Introduction

[2]   Our ability to model reasonably the tectonics and heat flow of icy satellites hinges on our understanding of the viscoelastic and plastic rheologies and microstructural evolution of the material comprising their icy outer shells. Although water ice is considered the dominant crystalline phase on the surface of most of the icy satellites, spectral data from Galileo's Near-Infrared Mapping Spectrometer (NIMS) indicate that, on Europa at least, there is more than just water ice present; the distorted and asymmetric water absorption bands observed in the NIMS spectra suggest H_2O in the form of a hydrated salt [*McCord et al.*, 1998]. *Dalton et al.* [2005] found that although no single compound matched the Europan spectra perfectly, spectra for those salts with the highest level of hydration, in particular,

$MgSO_4 \cdot 11H_2O$ (recently characterized and named "meridianiite" [*Peterson et al.*, 2007; *Fortes et al.*, 2008]), were the best fit to the observed data. Since it is well known that the addition of second phases can drastically alter the yield strength and fracture toughness of metals and ceramics, the presence of a non-ice material on the surface of such satellites requires that we consider fully the influence of a second phase on the mechanical properties of ice.

[3]   In this study, we conducted a suite of creep experiments on binary aggregates of ice I and MS11 at planetary conditions of stress, temperature and pressure. Here we present the results from these tests and compare them to results from pure polycrystalline ice I tested at the same conditions in the same apparatus. Samples were prepared using two different processing techniques in order to explore the sensitivity of the mechanical response to microstructural scale. The study differs from previous studies on two-phase ice-salt hydrate aggregates [*Durham et al.*, 2005] in that, instead of mechanically mixing two solid phases, all samples in this study were formed by eutectic solidification of a salt-bearing, homogeneous aqueous solution, consistent with icy shell formation and rejuvenation from an interior ocean. In addition to presenting our experimental data and resulting steady state constitutive equation, we provide

[1]Department of Geological Sciences, Brown University, Providence, Rhode Island, USA.
[2]Now at Earthquake Research Institute, University of Tokyo, Japan.
[3]Department of Earth, Atmospheric, and Planetary Sciences, Massachusetts Institute of Technology, Cambridge, Massachusetts, USA.
[4]U.S. Geological Survey, Menlo Park, California, USA.

Table 1. Thermodynamic-Microstructural Parameters and Steady State Creep Rates

Run[a]	Composition (Figure 2)	Specimen Preparation	P (MPa)	T (K)	σ_1 (MPa)	$\dot{\varepsilon}_{SS}$ (s^{-1})
526(2)	E′	bulk	50	240	5.45	1.51×10^{-7}
526(3)	E′	bulk	50	240	8.90	3.21×10^{-6}
526(4)	E′	bulk	50	240	12.40	1.96×10^{-5}
526(5)	E′	bulk	50	250	7.00	4.95×10^{-5}
527(1)	E	bulk	50	240	5.41	1.02×10^{-6}
527(2)	E	bulk	50	240	8.90	1.98×10^{-5}
527(3)	E	bulk	50	240	11.40	1.06×10^{-4}
B1(2)	E	bulk	0.1	240	1.85	1.04×10^{-8}
B1(4)	E	bulk	0.1	240	3.69	4.57×10^{-8}
B1(5)	E	bulk	0.1	240	4.59	1.40×10^{-7}
B1(6)	E	bulk	0.1	240	5.45	2.60×10^{-7}
B1(7)	E	bulk	0.1	240	6.26	5.20×10^{-7}
B1(8)	E	bulk	0.1	240	6.59	1.49×10^{-6}
B1(9)	E	bulk	0.1	240	6.74	2.89×10^{-6}
B2(3)	E	bulk	0.1	240	2.39	1.21×10^{-8}
B2(4)	E	bulk	0.1	240	3.19	2.00×10^{-8}
B2(5)	E	bulk	0.1	240	3.98	3.50×10^{-8}
B2(6)	E	bulk	0.1	240	4.77	6.90×10^{-8}
B2(7)	E	bulk	0.1	240	5.54	1.28×10^{-7}
B2(U)	E	bulk	0.1	240	3.93	2.71×10^{-8}
B3(1)	E	bulk	0.1	250	0.79	6.77×10^{-9} [b]
B3(2)	E	bulk	0.1	250	1.58	1.21×10^{-8}
B3(3)	E	bulk	0.1	250	2.33	5.07×10^{-8}
B3(4)	E	bulk	0.1	250	3.06	1.50×10^{-7}
B3(U)	E	bulk	0.1	250	1.52	1.16×10^{-8}
B4(1)	E	bulk	0.1	240	0.79	1.64×10^{-9} [b]
B4(2)	E	bulk	0.1	240	1.59	3.60×10^{-9}
B5(1)	E	bulk	0.1	230	0.83	7.40×10^{-10} [b]
B5(2)	E	bulk	0.1	230	1.67	1.31×10^{-9}
B5(3)	E	bulk	0.1	230	3.34	4.27×10^{-9}
B5(4)	E	bulk	0.1	230	4.17	7.87×10^{-9}
B5(5)	E	bulk	0.1	230	5.83	7.37×10^{-8}
B6(1)	E	droplet	0.1	240	0.81	2.40×10^{-8} [b]
B7(1)	E	droplet	0.1	230	1.75	5.11×10^{-9}
B7(2)	E	droplet	0.1	230	3.47	1.73×10^{-8}
B7(3)	E	droplet	0.1	230	4.32	2.64×10^{-8}
B7(4)	E	droplet	0.1	230	5.17	4.68×10^{-8}
B7(5)	E	droplet	0.1	230	5.99	8.42×10^{-8}
B7(6)	E	droplet	0.1	230	6.77	1.63×10^{-7}
B8(1)	E	droplet	0.1	250	0.83	2.64×10^{-8} [b]
B8(2)	E	droplet	0.1	250	0.98	3.52×10^{-8}
B8(3)	E	droplet	0.1	250	1.14	5.68×10^{-8}
B8(4)	E	droplet	0.1	250	1.57	2.87×10^{-7}
B8(5)	E	droplet	0.1	250	1.80	7.73×10^{-7}
B8(6)	E	droplet	0.1	250	1.94	1.35×10^{-6}
B9(1)	E	droplet	0.1	240	1.66	5.64×10^{-8}
B9(2)	E	droplet	0.1	240	2.95	2.13×10^{-6}

[a]Samples tested on the high-pressure apparatus are numbered 526 and 527 to follow the numbering protocol of that apparatus. Samples tested at ambient pressure are numbered B1–B9. Various stress increments for each sample are in parentheses. Generally, stress was increased with each increment, except those noted as U, which were decreased in stress.
[b]Samples at this stress level did not achieve true steady state.

microstructural analyses that inform our interpretation of the deformation behavior of the eutectic aggregates. We conclude by exploring implications of our findings for lithospheric strength of icy bodies of the outer solar system.

2. Experimental Methods

2.1. Sample Preparation–Microstructure

[4] Samples used in this study were crystallized from a homogenous liquid solution with a bulk composition equal to that of the stable H_2O–MS11 eutectic ($C_E = 17.28$ wt % MgSO₄), with the exception of one sample (526 in Table 1) in which a composition equal to that of the metastable eutectic between ice I and MgSO₄ • 7H₂O (epsomite; "MS7") was used ($C_{E'} = 19.55$ wt % MgSO₄; Figure 1). Sample microstructures have been controlled through two methods of sample fabrication: bulk solidification and droplet solidification. The bulk solidification method, fully described by *McCarthy et al.* [2007a], involves cooling a single volume (~5 mL) of liquid solution in a bath at a constant temperature (T = 268.5(±0.3) K), which lies below the eutectic isotherm (T_E = 269.6 K) but above the H_2O–MS7 metastable eutectic isotherm ($T_{E'}$ = 268 K). By maintaining the temperature between these two isotherms, we ensured growth of the stable crystalline phases. The solution was contained in a Pyrex™ test tube that was prescored along its length to allow fracturing of the tube and retrieval of the specimen after freezing. Specimens for mechanical testing were sectioned from the middle of the retrieved sample to avoid any compositional variations sometimes characteristic of the top and bottom of the as-frozen samples [*McCarthy et al.*, 2007b]. Samples made via bulk solidification developed classical ("regular lamellar") eutectic microstructure consisting of lamellae (~5–15 μm wide) of pure MS11 and pure ice I, as well as regions of a more complex, labyrinthine microstructure ("complex regular") in which MS11 and ice I form interconnected networks (Figure 2; see also section 2.3) [*Croker et al.*, 1973; *McCarthy et al.*, 2007a]. Regions with common microstructural orientation are called colonies. In Figure 2b the obvious feature on the diagonal is the boundary between two colonies, the topmost of which displays regular lamellar structure, whereas the bottom colony is complex regular. The morphological instabilities in the hydrate phase of the lamellar colony demonstrate that this system is on the boundary between these two eutectic morphologies. In samples made via bulk solidification the colonies vary in size, but are generally >200 μm wide with aspect ratios that
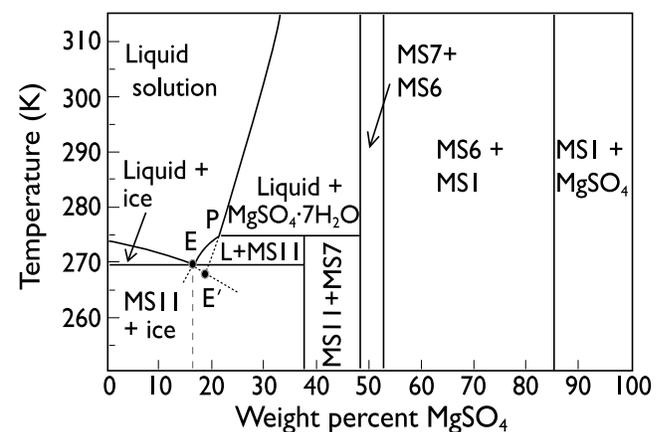
Figure 1. Equilibrium phase diagram for H_2O-MgSO₄ at P = 1 atm. The eutectic isotherm for the stable equilibrium L = ice I + MS11 occurs at 269.55 K and corresponds to a liquid composition of ~17.3 wt % MgSO₄ (point E). The metastable eutectic (L = ice I + MS7; point E′) occurs at ~268 K and a liquid composition of ~19.55 wt % MgSO₄. (Diagram adapted from *Hogenboom et al.* [1995] and *Peterson and Wang* [2006].)
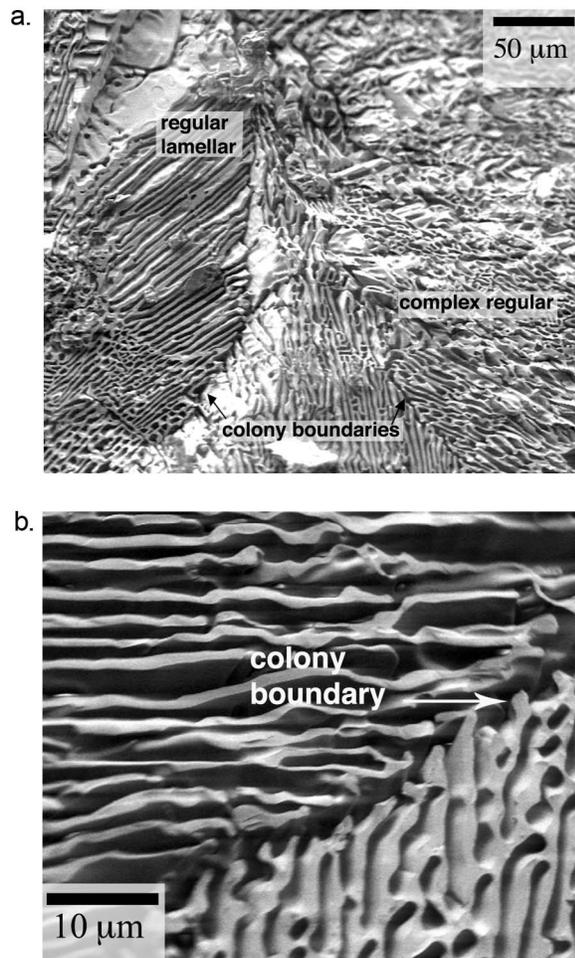
Figure 2. SEM-SEI images of fresh surfaces of ice I-MS11 aggregates prepared by bulk solidification ($T \cong 268$ K) of a homogeneous liquid solution of eutectic composition (17.3 wt % MgSO$_4$). (a) Low-magnification image showing a combination of alternating lamellae of ice and hydrate ("regular lamellar") and a maze-like, "complex regular" microstructure. (b) High-magnification image of a colony boundary. In these images, much of the ice has sublimated such that the hydrate phase stands in relief and the ice phase is in the recesses. The gap thus indicates that the colony boundary is predominately ice, with intrusions from the hydrate phase acting as potential obstacles to colony boundary sliding (CBS).

fine spray with mean droplet diameter of ~50 μm. The spray nozzle has an orifice diameter of ~0.5 mm and was positioned several centimeters above, and pointed directly at, a reservoir of liquid nitrogen (LN; 77 K). The droplets of eutectic solution solidified on contact with the LN, forming a glass due to sluggish diffusion kinetics in the solution at such a large undercooling [*Murray and Bertram*, 2008]. The vitreous state of the solidified droplets was confirmed by nuclear magnetic resonance (NMR): NMR revealed a stretched exponential distribution of the spin-lattice relaxation rate, which is characteristic of a glass [e.g., *Angell et al.*, 2000]. The slurry of liquid nitrogen and particles was then sieved so as to collect vitreous H$_2$O-MgSO$_4$ particles <25 μm in diameter. These fine particles were then hot-pressed under a roughing-pump vacuum (~0.1 Pa) in a stainless steel cylindrical die at 195 K (~0.73T_E), employing a nominally hydrostatic compaction stress of ~100 MPa that was maintained for 2 h. During this processing, in addition to aggregate densification, there was a phase change from the vitreous to the polyphase crystalline state via nucleation and solid-state diffusion. This sample preparation method yielded a uniform colony size of <25 μm (Figure 3). As with the bulk solidification method, the colonies are further subdivided into separate phases: in some cases the hydrate phase forms an interconnected network as shown in Figure 3b; in other cases, it forms rods and blades in an ice matrix. For samples prepared via this method, the widths of lamellae are 0.5–3.0 μm, and the boundaries between colonies are, similar to the bulk-solidified material, dominated by the ice phase, although within this boundary there can be found dispersed hydrate particles.

2.2. Mechanical Testing

[6] Compression creep experiments were conducted on a total of eleven samples using two different apparatus. The first was a cryogenic gas medium deformation apparatus that maintains temperature stability to within ±0.5 K at all test temperatures [*Durham et al.*, 1988]. Cooling is accomplished by passing liquid nitrogen through copper coils immersed in an ethanol bath around the pressure vessel. Temperature is monitored by types J and K thermocouples located in the bath and in the steel loading piston in contact with the sample. The temperature accuracy is that of the precision of the thermocouples, ±1 K. Experiments were conducted at $230 \leq T$ (K) ≤ 250 with nitrogen gas providing a hydrostatic confining pressure ($P = 50$ MPa). Differential stresses were $5.4 \leq \sigma$ (MPa) ≤ 12.4. Each cylindrical sample measured 25.4 mm in diameter and was encapsulated in an indium jacket that served as a plenum between the sample and the pressurized N$_2$. A motor-driven, axial piston supplied the load, which was measured by a "semi-internal" load cell. Strain was calculated using the instantaneous position measured by external displacement transducers on the piston. This apparatus can record strain rates as low as 2×10^{-8} s^{-1} [*Durham et al.*, 2001].

[7] The second instrument used was a high-resolution, ambient pressure, deadweight creep rig fitted with a cryostat that controlled temperature to ±0.5 K at ≤233 K and to ±0.25 K at >233 K [*Goldsby and Kohlstedt*, 2001]. The precision of the temperature is that of the copper constantan (type T) thermocouples, ±1 K, which are embedded in ceramic platens in contact with the ends of the sample.

range from two to six. Colony boundaries are dominated by ice I, though a roughness can be perceived, consisting of the penetration of hydrate lamellae from the adjoining colonies into the boundary region (Figure 2b).
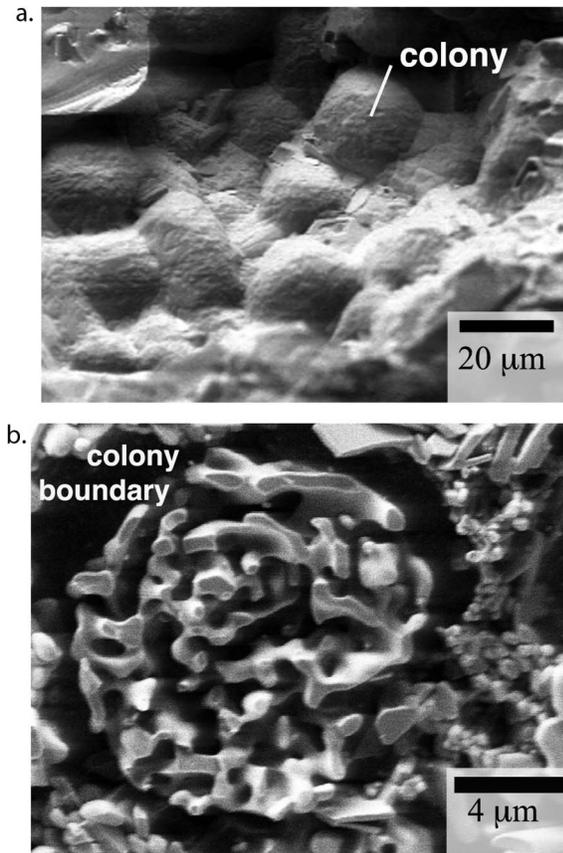
[5] Specimens with a finer-scale microstructure were fabricated by droplet solidification [e.g., *Turnbull*, 1952; *Wood and Walton*, 1970; *Goldsby and Kohlstedt*, 1997], followed by hot pressing. To minimize droplet size, liquid solution was introduced by pneumatic nebulization, which uses compressed air (~1.1 MPa) flowing through a Bernoulli effect nozzle to create a vacuum that siphons the liquid (~100 mL in 2 h) through a capillary tube and generates a

Figure 3. SEM-SEI images of ice I-MS11 samples obtained by the droplet solidification-hot-pressing technique. (a) The polyhedral entities are small (<25 μm) colonies that have primarily ice on the colony boundaries. (b) Taken after most of the ice had sublimated, revealing the complex network of ice and hydrate inside each colony. The wide, subcircular gap Figure 3b is a (sublimated ice) colony boundary.

Cylindrical samples for this instrument measured 10 mm in diameter and were tested at $230 \leq T$ (K) ≤ 250. Stresses explored ranged from $0.8 \leq \sigma$ (MPa) ≤ 6.8, with a resolution ~0.1 MPa. Changes in sample length were determined from measurements of the changes in distance between the ceramic platens in contact with the specimen ends using an LVDT-based extensometer. The resolution of this apparatus allows experiments at strain rates as slow as 1×10^{-8} s^{-1} [*Goldsby and Kohlstedt*, 2001].

[8] The use of the two different apparatus confers several advantages. First, it allows us to increase the range of conditions explored. The confining pressure of the first apparatus allows for higher stresses without fracture while the deadweight apparatus allows better accuracy and precision of stress, especially at low stress. Using the two apparatus also provides a check on internal consistency of the mechanical response of the materials, and also provides us with the opportunity to compare directly our new results with those from two seminal studies on polycrystalline pure ice [*Durham et al.*, 2001; *Goldsby and Kohlstedt*, 2001], experiments that were performed using the identical two apparatus. All creep tests in this study were performed as

step tests, which means that each load was applied to the sample until a nominal steady state creep rate was achieved and the next load was then applied. In most cases the tests were continued until the total accumulated strain of a specimen reached ~0.20. The thermodynamic and microstructural conditions for all experiments are listed in Table 1.

2.3. Microstructural Analyses

[9] Microstructural examination of predeformed and post-deformed specimens was conducted with a Leo 982 Macro field emission scanning electron microscope (FESEM) fitted with a Gatan Alto 2100 cryogenic preparation and coating station. The station permits a fresh fracture surface to be created under vacuum at $T < 100$ K that is then imaged at a low accelerating voltage of 2 kV using secondary electrons. Ice sublimates at a faster rate than does the hydrate in the vacuum of the SEM, ostensibly etching the samples to reveal the two-phase microstructure. Where ice is still present in the SEM images, it has a characteristic etch-pitted appearance [*Cross*, 1969]. Sublimation rates of ice in the SEM are known to be higher still at grain boundaries because these are regions of relatively high energy [e.g., *Cullen and Baker*, 2001]. As a result, grain boundary channels, or troughs, are formed, which become more pronounced as sublimation proceeds.

3. Experimental Results

3.1. Transient Response

[10] The rheological behavior of the eutectic aggregates has been evaluated following the analysis of *Andrade* [1910; cf. *Duval*, 1976; *Cooper*, 2002], in which time domain viscoelasticity constitutes a sum of elastic (el), anelastic (a; i.e., transient) and steady state (pl; i.e., plastic) strains, respectively:

$$\varepsilon(t) = \varepsilon_{\mathrm{el}} + \varepsilon_{\mathrm{a}} + \varepsilon_{\mathrm{pl}} = \sigma\left(\frac{1}{E} + \beta t^p + \frac{t}{\eta_{\mathrm{ss}}}\right), \qquad (1)$$

where E is Young's modulus, β is a constant, p ranges between 1/3 and 2/3 [cf. *Weertman and Weertman*, 1975], and η_{ss} is the steady state effective viscosity. The experimental data and corresponding Andrade model fit strain curves for bulk-solidified specimens tested at ambient pressure and at three different temperatures are shown in Figure 4. In order to avoid any influence of previous strain history [e.g., *Andrade*, 1952], each of the three curves corresponds to the first applied stress of its run. In each case, steady state was not reached in the time indicated (8 × 10⁴ s = 22.2 h) for these combinations of temperature and low stress (0.8 MPa). Instead, strain rates decrease until an apparent threshold has been reached (at about 25 h for the specimen deformed at 240 K, for example), at which point our capability of characterizing strain rate is exhausted and the strain versus time curve appears horizontal. A plot of strain rate versus strain at low stress does not achieve a constant rate and instead continues to decrease indefinitely. Thus, the fitted parameters for $\dot{\varepsilon}_{\mathrm{ss}}(= \sigma/\eta_{\mathrm{ss}})$ at low stresses are negligible, and so values for $\dot{\varepsilon}_{\mathrm{ss}}$ are not indicated in Figure 4. The Young's modulus, $E = 12.9$ GPa, used for these analyses was calculated by taking the average of the Voigt and Reuss mixing models of the temperature-compensated values for ice ($E = 9.5$ GPa) and for epsomite
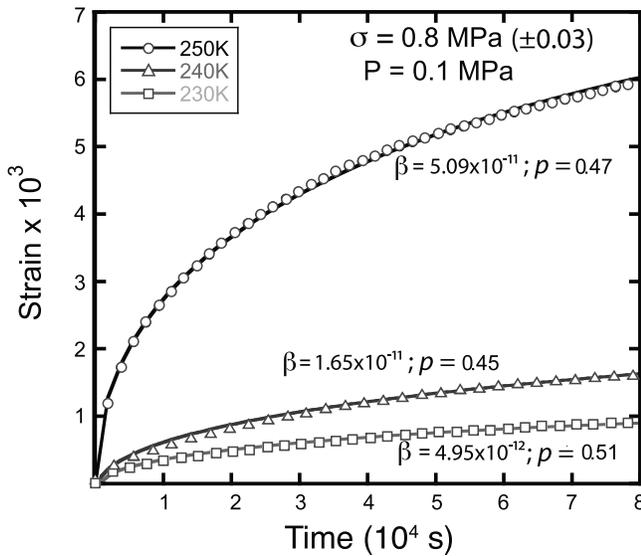
Figure 4. Compressive creep data (strain versus time at a constant differential stress of 0.8 MPa) for coarse colony size H_2O-$MgSO_4$ eutectic aggregates (bulk solidification) as a function of temperature. The open symbols represent the observed strain response, and the solid curve is the best fit to the Andrade model (equation (1)) for which the relevant parameters are noted. A long-duration, decelerating transient creep characterizes the approach to a steady state, though at the conditions here, the eutectic material has a steady state strain rate that is below the resolution of our apparatus ($<10^{-9}$ s^{-1}).

(MS7; E = 22.5 GPa). The latter value was used because, although there do not yet exist elastic modulus data for MS11, based on measurements of bulk modulus, the Young's moduli of MS7 and MS11 are anticipated to be nearly identical (A. D. Fortes, personal correspondence, 2008). The Reuss isostress value, E_R = 13.9 GPa, is in excellent agreement with the Young's modulus obtained from a separate set of cyclic loading experiments on these same materials at 0.1 Hz and 240 K (E = 13.8 GPa (C. McCarthy et al., manuscript in preparation, 2011)). Although the fit of the plastic portion of the model ($\sigma t/\eta_{ss}$ in equation (1)) only takes a resolvable, nonzero value (given experimental constraints), when the applied stress is larger than ~1 MPa, Figure 4 shows that, even at low stress, the elastic and anelastic portions of the model provide a very good fit to the data.
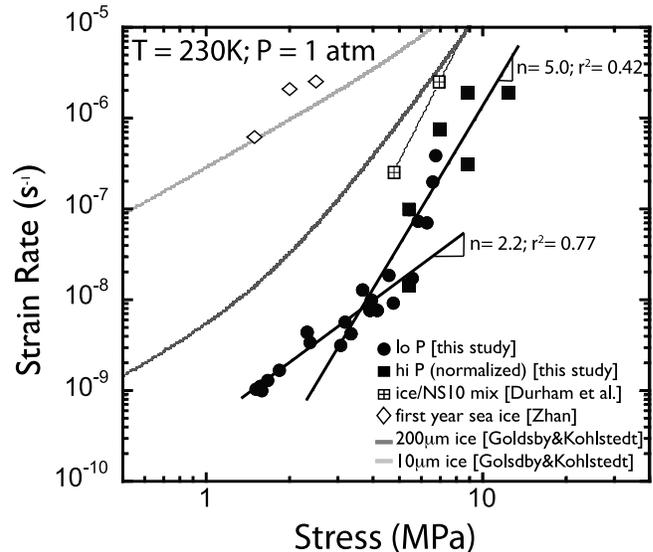
3.2. Steady State Response of Coarse Colony Size Samples

[11] The steady state creep behavior of pure polycrystalline ice has been studied extensively, and the relationship between strain rate, $\dot{\varepsilon}_{ss}$ (the subscript denoting steady state), and differential stress, σ, is generally quantified by the semiempirical power law:

$$\dot{\varepsilon}_{ss} = A \frac{\sigma^n}{d^q} \exp\left(-\frac{\Delta H_0 + PV^*}{RT}\right),$$ (2)

where A is a factor associated with aspects of microstructure (exclusive of grain size), chemical potentials and geometry, n and q are constants that reflect the (power law) sensitivities to stress and grain size (d), respectively, P is pressure, ΔH_0 and V^* the activation enthalpy at ambient pressure and activation volume, respectively, and RT has the usual meaning [e.g., *Frost and Ashby*, 1982; *Duval et al.*, 1983; *Weertman*, 1983; *Jacka*, 1984; *Louchet*, 2004].

[12] In Figure 5, steady state strain rate is plotted versus differential stress (normalized to T = 230 K and P = 1 atm) for coarse colony size samples made by bulk solidification. The high-pressure data were normalized from a confining pressure of 50 MPa to ambient pressure using the published activation volume for water ice (V^* = −13 cm³ mol⁻¹) [*Durham et al.*, 1997]. Apparent stress exponents (n from equation (2)) have been determined using linear regression analysis of the steady state data (from Table 1). Clearly, a single power law exponent is not adequate to describe the relationship between stress and strain rate: at least two distinct creep regimes can be identified. At low stress (<4 MPa), a creep regime is observed that is characterized by a stress exponent $n \approx 2.2$ and an activation enthalpy ΔH =

Figure 5. Steady state creep response of coarse colony size ice I-MS11 eutectic aggregates (bulk solidification) tested at P = 0.1 MPa (circles) and P = 50 MPa (squares). The data have been normalized to T = 230 K and P = 0.1 MPa using activation enthalpies calculated from this study and the published value for creep activation volume for pure ice. The data are compared to steady state responses of pure ice [*Goldsby and Kohlstedt*, 2001] having grain sizes similar to the eutectic colony size (~200 μm) and to the eutectic lamellar spacing (~10 μm). Also plotted are the data from a mechanical mixture of ~100 μm grains of ice and $Na_2SO_4 \cdot 10H_2O$ ("NS10") [*Durham et al.*, 2005] at the hydrate volume fraction (0.34) equivalent to the bulk composition of the eutectic samples in this study and from naturally occurring first year sea ice [*Zhan*, 1993]. Error in the data is associated with the inability to measure stress directly, which is affected by friction on pistons. The error is likely greatest at low stress (i.e., 1–2 MPa) but would not exceed 10%, which is approximately the size of the symbols.
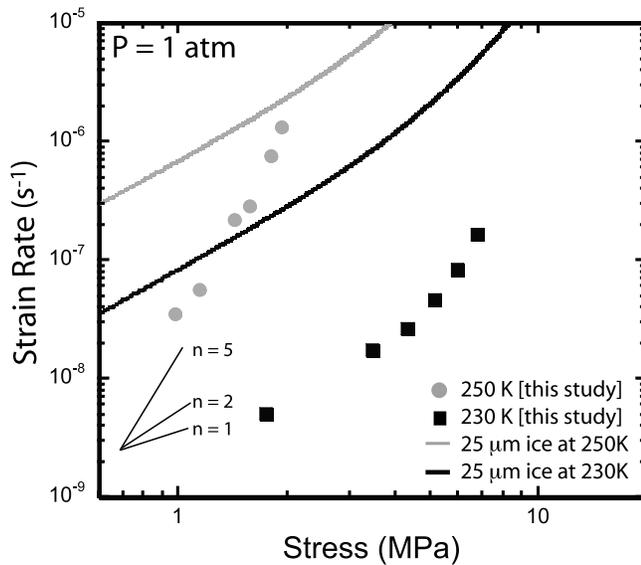
Figure 6. Steady state creep response for fine colony size samples of eutectic ice I-MS11 at 230 K and 250 K and P = 0.1 MPa. The data are compared to the flow law for polycrystalline ice [*Goldsby and Kohlstedt*, 2001] with a grain size similar to the size of the eutectic colonies.

55.7 kJ mol^{-1}, where $\Delta H = \Delta H_0 + PV^*$ in equation (2). At higher stress, a transition occurs to a creep regime with n ≈ 5.0. The activation enthalpy measured in this regime is 90.3 kJ mol^{-1}.

[13] Although the mechanical properties of pure MS11 are not yet characterized, an estimate of its properties relative to ice can be argued. MS7 is known to have an effective viscosity at least 100 times that of pure ice [*Durham et al.*, 2005]. With MS11 possessing a smaller Burgers vector ($|\vec{b}| = 0.675$ nm at 250 K [*Fortes et al.*, 2008]) and lower melting temperature ($T_m = 273.75$ K) than MS7 ($|\vec{b}| = 0.685$ nm; $T_m = 321.55$), we can expect pure MS11 to be somewhat less viscous than MS7 but still distinctly more viscous than polycrystalline ice ($|\vec{b}| = 0.450$ nm for basal slip). Although no experimental data exist for mixtures of MS11 and ice, on Figure 5 we plot the data from a mechanical mixture of Na$_2$SO$_4\cdot$10H$_2$O (0.34 volume fraction) and water ice [*Durham et al.*, 2005] and from first year sea ice (normalized to T = 230 K using the subsolidus data and activation enthalpy $\Delta H = 55$ kJ mol^{-1} calculated by *Zhan* [1993]). Also plotted are the flow laws for pure polycrystalline ice with grain sizes of 200 and 10 μm [*Goldsby and Kohlstedt*, 2001]. The results show that at low differential stress (e.g., $\sigma < 5$ MPa) the coarse colony size eutectic aggregates have an effective viscosity that is at least an order of magnitude greater than that of polycrystalline ice I with a grain size similar to the aggregate's colony size and several orders of magnitude greater than ice I with a grain size similar to the lamellar spacing of the eutectic material. The eutectic aggregates are also significantly stronger than the sea ice. Although the data from multiphase samples mixed in solid state [*Durham et al.*, 2005] display a similar n value (in equation (2)) to the eutectic aggregate at high stress, those samples, too, are less viscous than the samples of this study. Figure 5 also demonstrates that at ~6 MPa data from samples tested at ambient pressure

(shown as black circles) begin to deviate from power law behavior and instead ramp up to an n of ~14. Modest extrapolation of this increasing stress sensitivity predicts that at ~8 MPa the eutectic aggregates would be ultimately weaker than the ice I aggregates with comparable grain size.

3.3. Steady State Response of Fine Colony Size Samples

[14] Creep data for eutectic samples prepared via the droplet solidification-hot-pressing method are shown in Figure 6. At low stress, the fine colony size samples have an apparent stress exponent n = 1.7–1.8 and an activation enthalpy $\Delta H = 72$ kJ mol^{-1}. At high stress, however, it can be seen that the stress exponent is not constant, but rather "power law breakdown" is observed, with its associated acceleration of stress sensitivity. Although the fine-scale eutectic samples are also more resistant to creep than pure ice with a grain size similar to the eutectic colony size at the conditions tested, at high temperature ($T = 250$ K) and high stress, the data curves from the eutectic samples increase sharply to approach that of pure ice and are predicted to cross at stresses below 10 MPa. At low differential stress, the fine colony size samples display a lower steady state viscosity than coarse colony size samples. For instance, at $\sigma = 2$ MPa and T = 230 K, the difference in effective viscosities is a factor of ~3.5 (Figure 7). This difference decreases with increasing stress until approximately 6 MPa, when the two data sets converge and cross. Although both data sets in Figure 7 demonstrate accelerated stress sensitivity, the curve from the coarse colony size samples approaches vertical, i.e., rate-insensitive plasticity, above 6 MPa. The onset of yielding thus occurs at a lower stress in coarse colony size samples than in fine colony size samples.
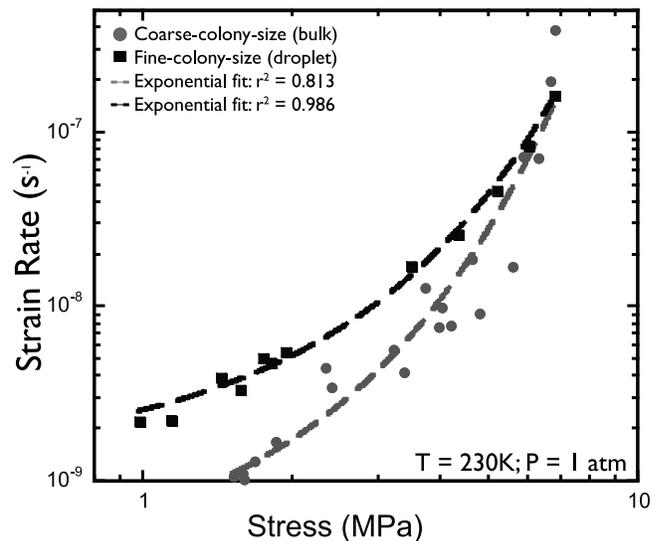
Figure 7. Steady state creep responses for both coarse and fine colony size samples at P = 0.1 MPa. The data have been normalized to 230 K using calculated activation enthalpies. The dashed curves represent the best fit for an exponential relationship to stress (equation (4)); the correlation coefficients r^2 are provided in the key. The accelerated stress sensitivity is consistent with yielding at ~6 MPa (for coarse colony size samples) and ~7 MPa (fine colony size).
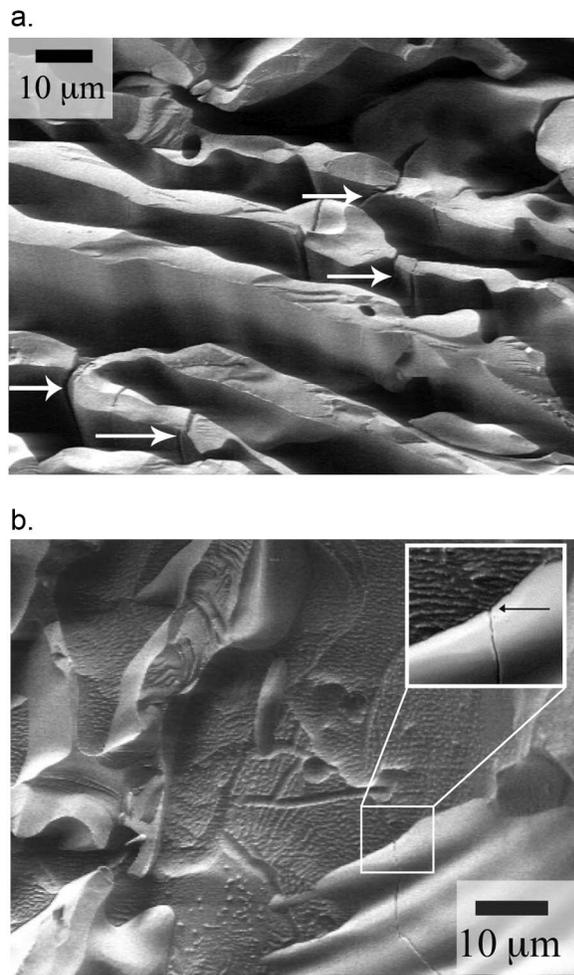
Figure 8. Postdeformation SEM-SEI images of a coarse colony size sample (B2 in Table 1) showing (a) cracks in the hydrate phase and (b) grain and subgrain boundaries within a mottled ice lamellae (the grain boundaries are indicated by the channels in the mottled phase), and the contrast between brittle fracture in the hydrate phase (smooth) and plastic flow in the ice phase (mottled). The inset in Figure 8b shows that ice has flowed into the small groove in the hydrate (arrow), which is the location of the fracture initiation in the hydrate.

3.4. Microscopy

[15] SEM-SEI images of a coarse colony size sample, postdeformation, are shown in Figure 8. The sample ("B2" in Table 1) was deformed at 240 K up to $\sigma = 5.54$ MPa. Straight to gently curved grain, and possibly subgrain, boundaries are visible within a single ice lamella (Figure 8b). Small fractures are visible in the hydrate grains with no indication of fracturing in adjacent ice grains, indicating a combination of plastic and brittle processes has occurred.

4. Discussion

[16] In a previous study, we demonstrated that the underlying physics of solidification of two-phase ice-salt systems from liquid solution is fully consistent with that of well-understood eutectic metals and ceramics [*McCarthy et al.*, 2007a]. In this study, we demonstrate that the same can be said for the steady state mechanical response of the eutectic ice-MS11 aggregates. Material scientists have long combined metals and dispersed ceramics in order to achieve enhanced mechanical response. Citing pearlitic steel as a classic example, the addition of a minority fraction of a higher-modulus phase (specifically, Fe_3C cementite) results in a significant increase in yield strength, but only at the expense of reduced fracture toughness. The findings from this present study indicate that the rheology of ice-MS11 eutectic aggregates can be understood fully in the context of creep, yielding and subcritical crack growth phenomenology of pearlitic steel and other, multiphase metals and ceramics [e.g., *Shi et al.*, 2002, 2003; *Darveaux*, 1992; *Lee and Stone*, 1994]. As such, we propose the following constitutive equation, which contains three contributing mechanisms responsible for plastic and anelastic flow in the ice-MS11 eutectic: (1) colony size sensitive (CSS) creep, which is composed of two serial processes: colony boundary sliding (CBS) and basal plane (bas) slip of dislocations; and (2) deformation within the colony, i.e., intracolony flow (IF):

$$\dot{\varepsilon}_{ss} = \dot{\varepsilon}_{CSS} + \dot{\varepsilon}_{IF} = \left(\frac{1}{\dot{\varepsilon}_{bas}} + \frac{1}{\dot{\varepsilon}_{CBS}}\right)^{-1} + \dot{\varepsilon}_{IF}. \qquad (3)$$

The CSS and IF mechanisms are kinetically parallel: the mechanism that dominates at a given set of (σ, T, P) conditions is the one that most quickly relieves the stored elastic energy, that is, the one that produces the greatest rate of strain. Phenomenologically, for a given microstructure over a given range of conditions, some mechanisms may not be observed. Further, the transition from one mechanism to the next (with increasing stress) can appear continuous in stress versus strain rate space. The terms in equation (3) are presented below in order of their predominance as differential stress increases at constant temperature.

[17] At sufficiently low stress, deformation is fully ductile and is primarily occurring within the ice phase, which is the softer of the two. The dominant mechanism is CSS creep. In order to satisfy compatibility issues at colony boundaries and irregularities within the area of the boundary (i.e., to have deformation without voids), colony boundary sliding is accompanied by some form of deformation within the colonies [e.g., *Hart*, 1967]. This serial relationship between the two mechanisms, in which the slower of the processes controls the strain rate, is analogous to that observed for grain-size-sensitive (GSS) creep in pure, polycrystalline ice [*Goldsby and Kohlstedt*, 2001; *Durham et al.*, 2001], where the necessary intragranular deformation is accomplished by easy slip of dislocations on the basal plane. However, in the present study the scale of the eutectic microstructure, which differs widely because of differences in fabrication history, influences the stress at which the transition from dislocation slip to colony sliding occurs.

[18] In the case of the coarse colony size samples, a strain rate associated with basal slip within favorably oriented ice lamellae is observed. The stress exponent ($n = 2.2$) and activation enthalpy $\Delta H = 55.7$ kJ mol^{-1} measured for coarse colony size samples at low stress (<4 MPa) are in excellent agreement with data reported for easy slip on basal planes in single crystals of ice ($n = 2$–2.5; $\Delta H = 60$ kJ mol^{-1} [*Jones and Glen*, 1969]). However, unlike pure ice, the data for the

eutectic aggregates do not shallow out at intermediate stress to a CBS rate-limited step. Rather, samples with lamellar microstructure show a smooth transition from basal-slip-limited dislocation motion (n = 2.2) to a stress exponent ($n \approx 5$) associated with intracolony flow at intermediate stress. Consistent with the behavior of similarly coarse-scale lamellar eutectic metal aggregates [e.g., *Cline and Lee*, 1970], there is little to no CBS in the coarse lamellar samples of this study.

[19] The same cannot be said for the fine colony size samples. CBS, which is a form of superplasticity, is known to be enhanced when colonies are equiaxed and have same-phase boundaries [e.g., *Mei and Morris*, 1992]. As shown in Figure 3a, the fine eutectic aggregates made by droplet solidification have uniformly subspherical colonies with primarily ice on the colony boundaries (thus an ice-ice boundary); but dispersed hydrate particles are found on this boundary. Indeed, the data show that low-stress (<4 MPa at 230 K) rheology of the fine-colony samples is rate controlled by CBS. The stress exponent (n = 1.7–1.8) is fully consistent with GSS creep in pure ice that is rate limited by grain boundary sliding (GBS) [*Goldsby and Kohlstedt*, 1997]. That the apparent activation enthalpy for this regime (ΔH = 72 kJ mol^{-1}) is larger than that reported for pure ice (ΔH = 49 kJ mol^{-1}) is likely due to an enhancement of creep rate in the 250 K data. *Goldsby and Kohlstedt* [2001] observed an increase in activation enthalpy for the n = 1.8 regime to ~190 kJ mol^{-1} for T > 255 K (T/T_m = 0.93) that they attributed to premelting at grain boundaries. The onset of similar surface (interfacial) melting is likely occurring in samples from this study measured at 250 K (T/T_E = 0.93), and thus the high activation enthalpy that we calculate is not unreasonable.

[20] Although deformation in the CSS regime is primarily occurring in the soft ice phase, both the coarse and fine colony size eutectic samples display viscosities significantly greater than pure ice at comparable grain sizes. The increased yield strength of the ice-hydrate eutectics can be attributed to several strengthening mechanisms. The most significant of these is boundary hardening, which, in the CSS regime, is caused by a decrease in the free path movement of glide dislocations in the ice phase [*Hertzberg*, 1996]. The disparity in lattice spacing and elastic properties between the ice and hydrate phases means that dislocations pile up and create high stress concentrations at ice-hydrate heterophase boundaries, which is known to occur even in pure ice, i.e., at grain boundaries, at high enough strain rates [e.g., *Cole*, 1988]. In coarse colony size samples, dislocations on basal planes within individual ice lamellae interact with heterophase boundaries, whereas in fine colony size samples, dislocations facilitating CBS will interact with dispersed hydrate particles lodged in the ice-ice boundary. The difference in yield strength between the coarse colony size and fine colony size samples can partly be attributed to the reduced hydrate size, i.e., smaller particle size minimizes pileup [e.g., *Dieter*, 1986]. However, the more significant reason for the difference in strengths is colony boundary sliding. In the CSS regime, the fine colony size samples are essentially superplastic.

[21] In addition to boundary hardening, eutectic materials are also subject to solid solution strengthening. In multi-phase metals, for instance, solute atoms create lattice dis-

tortion that impedes the motion of dislocations and increases yield strength. However, studies on ice doped with HF, NH₃ [*Nakamura and Jones*, 1973], HCl, [*Nakamura and Jones*, 1970], and H₂SO₄ [*Li et al.*, 2009] find that soluble impurities at concentration between ~2 and 6 ppm instead effect a more rapid reorientation of dislocation-obstructing bonds, thereby *increasing* the mobility of dislocations and lowering viscosity [*Glen*, 1968; *Nakamura and Jones*, 1970; *Li et al.*, 2009], whereas concentrations less than 0.1 ppm were found to have no effect on deformation rate [*Paterson*, 1991]. The upper limit of solubility of (SO₄)²⁻ in ice is estimated to be less than 1 ppm [*Dominé and Thibert*, 1995]. At this level, the effect of solid solution strengthening (or weakening) is expected to be very small compared to boundary hardening effects.

[22] In the IF regime, boundary hardening is associated with the increased local stress required to nucleate dislocations in the hydrate phase. As is the case in other lamellar microstructures, the tendency for the hydrate phase to plastically deform or to fracture in response to the glide plane pileup of dislocations is a function of scale [cf. *Langford*, 1977]. As a direct result of their fabrication histories, the microstructures of samples from this study have approximately an order of magnitude difference in scale, and thus a comparison of their flow strengths provides insight into the impact of hydrate thickness on deformation (Figure 7). At ~7 MPa the creep-flow strength curves of the two types of samples cross. Due to the extremely small size of the hydrate phase in the fine colony size samples, the hydrate is either bending elastically or is sufficiently thin to remain ductile (i.e., free of Griffith-type cracks), so that the sample deforms plastically to higher stress than the coarse colony size samples.

[23] Figure 8a demonstrates that significant microcracking of the MS11 phase occurred in coarse colony size samples deformed to even moderate stresses. As evidenced in the inset of Figure 8b, the ice phase has begun to flow into the tiny fractures that formed. This combination of brittle and ductile mechanisms at the microscale, while maintaining ductility at the macroscale, constitutes semibrittle flow, which is known to occur in a variety of geologic materials at appropriate (σ, T, P, microstructure) conditions [e.g., *Hirth and Tullis*, 1994; *Dell'Angelo and Tullis*, 1996; *White*, 2001]. Although there is no well-accepted constitutive relationship to describe partitioning between brittle fracture and plastic flow within the semibrittle regime, it is generally accepted that the increase in temperature sensitivity at the brittle-semibrittle transition and the increase in pressure sensitivity at the semibrittle-plastic transition results in a reduction of strength of each mechanism [e.g., *Evans et al.*, 1990] The high-stress response is thus significantly different from what is observed in studies on ice with suspended sand, for instance. In such studies, the silicate particles are infinitely harder than the ice matrix, causing dislocations to get tangled around the hard particles, increasing the creep rate and the yield strength [*Hooke et al.*, 1972]. Here, the brittle second phase eventually fractures, so that, like many composite materials, increased yield strength actually lowers the fracture toughness [cf. *Dieter*, 1986]. The well-known inverse relationship stems from the fact that with increased yield stress comes an increase in the probability of nucleating a critical crack.

[24] Many engineering and geologic materials in regimes of plastic yielding or semibrittle behavior display a break down in the power law relationship between stress and strain rate. Experimental data in these cases are better approximated by an exponential relationship of stress and strain rate [e.g., *Goetze and Evans*, 1979; *Karato*, 2008]. Indeed, the dashed curves in Figure 7 demonstrate that data from both scales of samples are well fit functionally by a simple exponential relationship of the form

$$\dot{\varepsilon} = A_1 \exp(\sigma) \exp\left(\frac{-\Delta H}{RT}\right) \qquad (4)$$

once the high-pressure data are removed. Here, the pre-exponential term A_1 is a constant that contains scaling information that is still poorly constrained. The other terms have the same meaning as in equation (2). Although exponential creep is less extensively studied, it is generally understood that it arises when nondiffusional creep mechanisms control the deformation [e.g., *Raj*, 2002].

[25] At this point, the pressure sensitivity of semibrittle behavior in ice-MS11 aggregates is unknown. That the high-pressure data (squares in Figure 5) maintain distinctly a power law relationship to 12 MPa (thus linear in appearance in log-log space), however, suggests that at the pressure of P = 50 MPa, distributed microcracking was prevented, or at least "delayed" in stress. Our data indicate that this is the case until very high differential stress was applied. Since a hydrostatic pressure of P = 50 MPa would not occur until a depth of ~40 km in an icy shell (at Europa's gravity), which is well within the warm ductile region, the suppression of brittle behavior by confining pressure is irrelevant in this planetary context.

[26] At high enough stresses, all samples, regardless of confining pressure or microstructure, can eventually experience a coalescence of cracks and/or cavitation, which leads to unstable cataclastic deformation, i.e., macroscopic faulting. Such behavior represents a full transition from distributed deformation into localized brittle fracture and is beyond the scope of this paper.

[27] Since creep viscosity of lamellar eutectics is (inversely) correlated with lamellar spacing [e.g., *Hyzak and Bernstein*, 1976; *Langford*, 1977; *Hertzberg*, 1996], it is worth considering the stability of the microstructure over time. As with any two-phase material, the H_2O-MgSO₄ system will tend toward coarsening in order to minimize the total interfacial free energy. The kinetics of coarsening in eutectic systems depends on the stoichiometry of the phases present and the morphology of the microstructure, as well as on the thermodynamic conditions by the following relationship:

$$D^\zeta - D_0^\zeta = K_0 \left[\exp\left(\frac{-E_A}{RT}\right)\right] t, \qquad (5)$$

where D and D_0 are, in this case, the interlamellar spacing at times t and 0, respectively, ζ is the phase size exponent, K_0 is a rate constant, E_A is activation enthalpy, and RT has the usual meaning [*Senkov and Myshlyaev*, 1986; *Jung and Conrad*, 2001]. Due to the extreme differences in crystal structures, there is only limited solid solubility between the ice and the sulfate-hydrate phases in this system, so that

coarsening of the lamellar eutectic is controlled by diffusion of solutes Mg^{2+} and $(SO_4)^{2-}$ at heterophase and grain boundaries. Therefore, in equation (5), ζ is 4 (as opposed to the cubic signature of systems with a dispersed second phase, where Ostwald ripening occurs [e.g., *Jung and Conrad*, 2001]); E_A is the activation energy for grain boundary diffusion in ice (38 kJ mol⁻¹ [*Frost and Ashby*, 1982]) and K_0 is determined by

$$K_0 = B\gamma c_0 \Omega w D_{gb} \qquad (6)$$

where B is a parameter related to volume fraction, γ is the heterophase boundary interfacial energy, $c_0 \approx \exp(-\Delta H_f/RT)$ is the equilibrium solute concentration near the grain boundaries in the absence of the second phase (ΔH_f is the enthalpy of fusion), Ω is the molecular volume, w is the grain boundary width and D_{gb} is the grain boundary diffusion coefficient. Although we do not have exact values for all of the parameters found in equation (6), we assume the following values as reasonable for the system H_2O-MgSO₄ at eutectic composition: $B = 2$; $\gamma = 80$ mJ m⁻² [*McCarthy et al.*, 2007a]; $c_0 = \exp(-6000$ J mol⁻¹/RT); $\Omega = 8.7 \times 10^{-5}$ m³ mol⁻¹; and $wD_{gb} = 8.3 \times 10^{-13}$ m³ s⁻¹ [*Frost and Ashby*, 1982]. Inserting these values into equation (6), we obtain the following range for K_0: $K_0 = 2 \times 10^{-24}$ m⁴ s⁻¹ at $T = 80$ K (e.g., the Europan surface temperature) to $K_0 = 3.5 \times 10^{-22}$ m⁴ s⁻¹ at $T = 269$ K (melting temperature at the base of a eutectic shell), which translates to a growth rate dD/dt (when $D_0 = 10$ μm) that ranges from 5×10^{-35} to 3.2×10^{-15} m s⁻¹. Such extremely slow estimated growth rates indicate that the fine eutectic microstructure observed in this study is particularly robust and so its effects on the mechanical response should not be ignored, even over geological time.

5. Planetary Implications and Conclusions

[28] The results of this study demonstrate the profound effect that microstructure has on the mechanical response of the two-phase aggregates. Because microstructural scale in eutectic aggregates is a direct result of thermodynamic conditions upon crystallization (as well as subsequent mechanical processing), it is ultimately the thermal and chemical histories of formation (and deformation) of an icy shell that are important in characterizing its strength. At this time, it is not well understood how the shells of various icy satellites originally formed or how they have been subsequently altered. In section 4 we found that eutectic coarsening kinetics predict the time needed for growth of ice lamellae from 10 μm to just 20 μm at Europan surface temperature would be on the order of 10^{22} years and at the warmest temperatures at the base of the shell would still be ~390 years. It is believed that dark albedo features on the surface in the complex networks and chaos regions on Europa, for example, likely correspond to recent crystallization of brine [*McCord et al.*, 1999]. It is in these regions, at least, that fine-scale eutectic microstructures could be present today.

[29] The mechanical and microstructural observations from this study indicate that a second phase in the context of a eutectic intergrowth microstructure makes a material that is both more resistant to creep and more brittle than pure ice.

The second phase promotes semibrittle behavior at high stress. Several lines of evidence point to this semibrittle behavior: (1) pressure sensitivity of the stress associated with yielding; (2) increased stress sensitivity of the strain rate; and (3) combined brittle and ductile features in post-deformation micrographs. The rheologic structure of a multiphase crust that can be inferred from such properties is notably different from that of a pure ice shell. In a planetary body, pressure and temperature are related to depth according to thermal and density gradients. Strength in the lithosphere increases with depth due to an increase in lithostatic pressure, but a temperature increase at greater depths decreases strength and promotes ductile flow. Strength profiles, or "envelopes," are used to estimate the transition from brittle to ductile behavior and analyze mechanical behavior with depth [e.g., *Brace and Kohlstedt*, 1980; *McNutt*, 1984; *Mangold et al.*, 2002]. In studies on Europa, the strength envelope for pure ice is used to model such features as topographic relaxation and buckling in the icy shell [*Dombard and McKinnon*, 2006; *Luttrell and Sandwell*, 2006]. The brittle portion of such a strength envelope is described by application of "Byerlee's rule" (Coulombic friction) to ice, which is a function of over-burden pressure [*Zoback and Townend*, 2001]:

Differential stress(compression)

$$\sigma_1 - \sigma_3 = -\rho g h (1 - F) \qquad (7)$$

Differential stress(tension)

$$\sigma_1 - \sigma_3 = -\rho g h (1 - F)/F, \qquad (8)$$

where ρ is density (930 kg m^{-3} for ice), g the gravitational acceleration (1.31 m s^{-2} on Europa), h is the depth in the ice layer, and the friction function F is defined by *Jaeger and Cook* [1979] as

$$F = \left(\sqrt{\mu^2 + 1} + \mu \right)^2, \qquad (9)$$

where μ is the coefficient of dynamic friction. The value of μ of ice was determined by *Beeman et al.* [1988] to be 0.69.

[30] The ductile portion of a strength envelope is obtained from experimental data. In the case of pure ice, this includes a grain-size-insensitive dislocation creep response at high stress and grain-size-sensitive GBS at low stress [*Durham et al.*, 2001; *Goldsby and Kohlstedt*, 2001]. Both are functions of temperature, which increases, in the Europa example, from ~80 K at the surface to T_m at the base of the ice layer. The temperature gradient is thus highly dependent on shell thickness. Figure 9a shows an example of a strength envelope for pure ice assuming a thermal gradient of 18 K
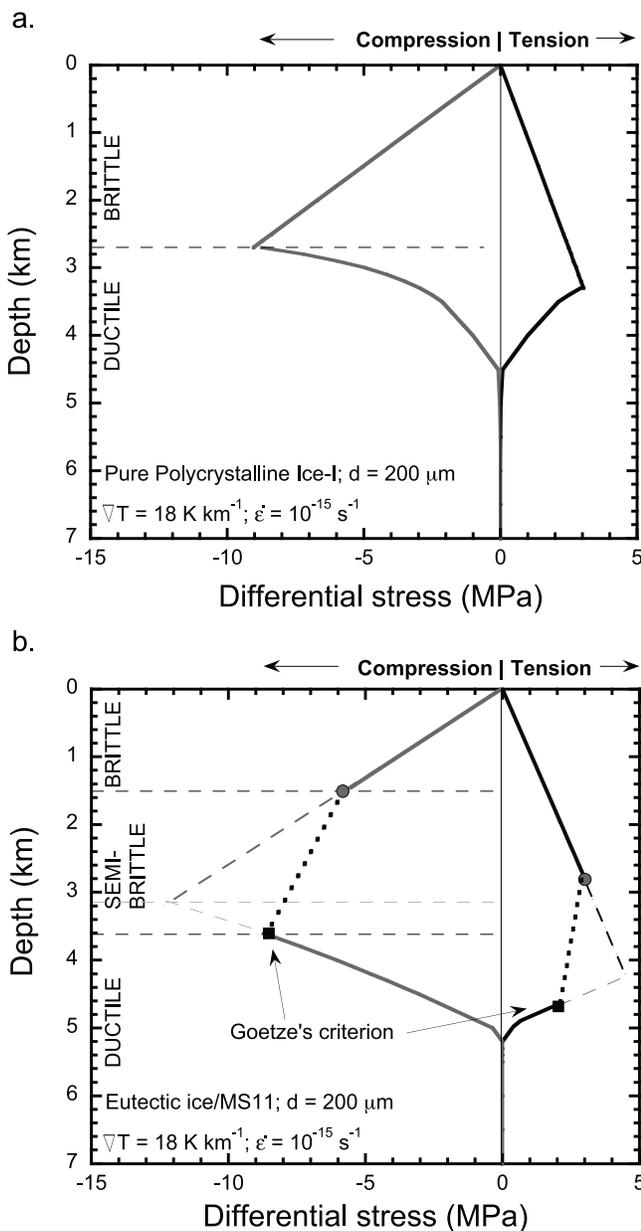
Figure 9. Strength envelopes for pure polycrystalline ice and for ice–MS11 eutectic. (a) Envelope for pure ice (compression negative) using assumptions from *Dombard and McKinnon* [2006], i.e., thermal gradient equal to 18 K km^{-1} and shortening rate of 10^{-15} s^{-1}. The brittle portion is defined by Coulombic friction (coefficient of dynamic friction of 0.69) with zero cohesion [*Beeman et al.*, 1988]. The ductile portion is defined by experimental creep studies combining dislocation mechanisms and GBS. The grain size is 200 μm. For these conditions, the brittle-ductile transition is ~2.7 km. (b) Envelope for ice-MS11 eutectic assuming the same thermal conditions and frictional law as in Figure 9a (with $\rho = 1130$ kg m^{-3} [*Spaun and Head*, 2001]) but instead employing the inelastic rheology of this study (the exponential form from Figure 7, i.e., equation (4), until the depth of 5 km, below which a power law was used). The upper bound of the semibrittle behavior is estimated at 5 times the frictional stress [*Kohlstedt et al.*, 1995] and the lower bound is estimated by Goetze's criterion. The blunting of the strength envelope by semibrittle behavior results in a shallower transition (~1.5 km) to plastic behavior and lowers the magnitude of compressional stress needed to saturate the envelope.

km^{-1} and a strain rate of 10^{-15} s^{-1} (estimated shortening rate for contractional folding [*Dombard and McKinnon*, 2006]).

[31] In contrast, we provide Figure 9b to demonstrate the effect on lithospheric strength of having a finely dispersed meridianiite second phase, consistent with eutectic solidification. Although the incoherent phase boundaries provide barriers to dislocation motion, they simultaneously provide nucleation sites for rampant microfracturing and make the material more flaw sensitive. Semibrittle behavior thus reduces the maximum strength in both the plastic and the brittle regimes, thereby blunting the ends of the strength envelope [e.g., *Scholz*, 1988]. This creates a transition from brittle to ductile behavior that occurs over a relatively wide region of semibrittle flow [e.g., *Kirby*, 1980; *Hirth and Tullis*, 1994; *He et al.*, 2003]. Although detailed laboratory information on the brittle to ductile transition (as a function of confining pressure) in ice-hydrate eutectic does not exist, estimates developed in geologic studies can be applied. The transition from semibrittle behavior to purely plastic flow occurs where the stress necessary for plastic flow is approximately equal to the effective confining pressure, that is, where the plastic yield stress is equal to $\sigma_1 - \sigma_3$, known as Goetze's criterion. *Kohlstedt et al.* [1995] estimate the transition from brittle behavior to semibrittle flow by assuming that limited plastic flow can occur when flow stress is less than 5 times the frictional stress (indicated by the circles on Figure 9b). Geological observations of rock deformed in the semibrittle regime indicate that this may even be an overestimate [*Karato*, 2008]. The result is that, despite being stronger than pure polycrystalline ice at very low stress, eutectic ice-MS11 deforming by a semibrittle mechanism (that is triggered by stress concentrations that form at the heterophase boundaries) will display a critical strength that is significantly lower than pure ice.

[32] In the above argument, it is not our desire to validate or invalidate specific geophysical assumptions, e.g., about the specific temperature gradient in the Europan shell, but rather to show that, all other things being equal, an icy crust composed of two-phase ice-salt hydrate eutectic material corresponds to a brittle layer nearly half the thickness of that calculated for a pure ice crust. More importantly, the semibrittle regime could serve to lower the magnitude of horizontal compression needed to saturate the strength envelope, making it easier to form morphological features in the shell such as contractional folds. One of the few surface features on Europa considered to be compressional in nature (and thus compensating for ubiquitous extensional features [*Prockter and Pappalardo*, 2000]) is topographic undulations like those at Astypalaea Linea (~69°S, 198°W) that require instabilities at higher stresses than believed to be possible in a shell of pure ice [*Dombard and McKinnon*, 2006]. Our study shows that the maximum strength of a semibrittle shell would be reduced to ~6 MPa, which is much more consistent with estimates of compressive stresses by nonsynchronous rotation [*Leith and McKinnon*, 1996]. Thus, our experiments and their extrapolation provide a plausible explanation for observed zones of weakness in the crust.

References

Andrade, E. N. D. (1910), On the viscous flow in metals and allied phenomena, *Proc. R. Soc. London, Ser. A, 84*, 1–12.

Andrade, E. N. D. (1952), The flow of metals, *J. Iron Steel Inst. London, 171*, 217–228.

Angell, C. A., K. L. Ngai, G. B. McKenna, P. F. McMillan, and S. W. Martin (2000), Relaxation in glassforming liquids and amorphous solids, *J. Appl. Phys., 88*(6), 3113–3157, doi:10.1063/1.1286035.

Beeman, M., W. B. Durham, and S. H. Kirby (1988), Friction of ice, *J. Geophys. Res., 93*, 7625–7633, doi:10.1029/JB093iB07p07625.

Brace, W. F., and D. L. Kohlstedt (1980), Limits on lithospheric stress imposed by laboratory experiments, *J. Geophys. Res., 85*, 6248–6252, doi:10.1029/JB085iB11p06248.

Cline, H. E., and D. Lee (1970), Strengthening of lamellar vs. equiaxed Ag-Cu eutectic, *Acta Metall., 18*, 315–323, doi:10.1016/0001-6160 (70)90146-X.

Cole, D. M. (1988), Crack nucleation in polycrystalline ice, *Cold Reg. Sci. Technol., 15*, 79–87, doi:10.1016/0165-232X(88)90041-9.

Cooper, R. F. (2002), Seismic wave attenuation: Energy dissipation in viscoelastic crystalline solids, in *Plastic Deformation of Minerals and Rocks, Rev. Mineral. Geochem.*, vol. 51, edited by S. Karato and H. R. Wenk, pp. 253–290, Mineral. Soc. of Am., Washington, D. C.

Croker, M. N., R. S. Fidler, and R. W. Smith (1973), The characterization of eutectic structures, *Proc. R. Soc. London, Ser. A, 335*, 15–37, doi:10.1098/rspa.1973.0111.

Cross, J. D. (1969), Scanning electron microscopy of evaporating ice, *Science, 164*(3876), 174–175, doi:10.1126/science.164.3876.174.

Cullen, D., and I. Baker (2001), Observation of impurities in ice, *Microsc. Res. Tech., 55*(3), 198–207, doi:10.1002/jemt.10000.

Dalton, J. B., O. Prieto-Ballesteros, J. S. Kargel, C. S. Jamieson, J. Jolivet, and R. Quinn (2005), Spectral comparison of highly hydrated salts with disrupted terrains on Europa, *Icarus, 177*, 472–490, doi:10.1016/j.icarus.2005.02.023.

Darveaux, R. (1992), Constitutive relations for tin-based solder joints, *IEEE Trans. Compon. Hybrids Manuf. Technol., 15*(6), 1013–1024, doi:10.1109/33.206925.

Dell'Angelo, L. N., and J. Tullis (1996), Textural and mechanical evolution with progressive strain in experimentally deformed aplite, *Tectonophysics, 256*, 57–82, doi:10.1016/0040-1951(95)00166-2.

Dieter, G. E. (1986), *Mechanical Metallurgy*, 3rd ed., 372 pp., McGraw-Hill, New York.

Dombard, A. J., and W. B. McKinnon (2006), Folding of Europa's icy lithosphere: An analysis of viscous-plastic buckling and subsequent topographic relaxation, *J. Struct. Geol.*, doi:10.1016/j.jsg.2005.12.003.

Dominé, F., and E. Thibert (1995), Relationship between atmospheric composition and snow composition for HCl and HNO$_3$, in *Biogeochemistry of Seasonally Snow-Covered Catchments, Proceedings of a Boulder Symposium*, edited by K. Tonnessen, M. Williams, and M. Tranter, *IAHS Publ., 228*, 3–10.

Durham, W. B., S. H. Kirby, H. C. Heard, L. A. Stern, and C. O. Boro (1988), Water ice phases II, III, and V: Plastic deformation and phase relationships, *J. Geophys. Res., 93*, 10,191–10,208, doi:10.1029/JB093iB09p10191.

Durham, W. B., S. H. Kirby, and L. A. Stern (1997), Creep of water ices at planetary conditions: A compilation, *J. Geophys. Res., 102*, 16,293–16,302, doi:10.1029/97JE00916.

Durham, W. B., L. A. Stern, and S. H. Kirby (2001), Rheology of ice I at low stress and elevated confining pressure, *J. Geophys. Res., 106*, 11,031–11,042, doi:10.1029/2000JB900446.

Durham, W. B., L. A. Stern, T. Kubo, and S. H. Kirby (2005), Flow strength of highly hydrated Mg- and Na-sulfate hydrate salts, pure and in mixtures with water ice, with application to Europa, *J. Geophys. Res., 110*, E12010, doi:10.1029/2005JE002475.

Duval, P. (1976), Lois de fluage transitoire ou permanent de la glace polycristalline pur divers etats de contrainte, *Ann. Geophys., 32*, 335–350.

Duval, P., M. F. Ashby, and I. Anderman (1983), Rate-controlling processes in the creep of polycrystalline ice, *J. Phys. Chem., 87*, 4066–4074, doi:10.1021/j100244a014.

Evans, B., J. T. Fredrich, and T.-F. Wong (1990), The brittle-ductile transition in rocks: Recent experimental and theoretical progress, in *The Brittle-Ductile Transition in Rocks: The Heard Volume, Geophys. Monogr. Ser.*, vol. 56, edited by A. G. Duba et al., pp. 1–20, AGU, Washington, D. C.

Fortes, A. D., I. G. Wood, and K. S. Knight (2008), The crystal structure and thermal expansion tensor of MgSO$_4$-11D$_2$O (meridianiite)

determined by neutron powder diffraction, *Phys. Chem. Miner.*, *35*(4), 207–221, doi:10.1007/s00269-008-0214-x.

Frost, H. J., and M. F. Ashby (1982), *Deformation-Mechanism Maps: The Plasticity and Creep of Metals and Ceramics*, 112 pp., Pergamon, Oxford, U. K.

Glen, J. W. (1968), The effect of hydrogen disorder on dislocation movement and plastic deformation of ice, *Phys. Kondens. Mater.*, *7*, 43–51.

Goetze, C., and B. Evans (1979), Stress and temperature in the bending lithosphere as constrained by experimental rock mechanics, *Geophys. J. R. Astron. Soc.*, *59*, 463–478.

Goldsby, D. L., and D. L. Kohlstedt (1997), Grain boundary sliding in fine-grained ice I, *Scr. Mater.*, *37*(9), 1399–1406, doi:10.1016/S1359-6462(97)00246-7.

Goldsby, D. L., and D. L. Kohlstedt (2001), Superplastic deformation of ice: Experimental observations, *J. Geophys. Res.*, *106*, 11,017–11,030, doi:10.1029/2000JB900336.

Hart, E. W. (1967), A theory for flow of polycrystals, *Acta Metall. Mater.*, *15*, 1545–1549, doi:10.1016/0001-6160(67)90185-X.

He, C., Y. Zhou, and Z. Sang (2003), An experimental study on semi-brittle and plastic rheology of Panzhihua gabbro, *Sci. China, Ser. D*, *46*(7), 730–742, doi:10.1360/03yd9064.

Hertzberg, R. W. (1996), *Deformation and Fracture Mechanics of Engineering Materials*, 4th ed., 144 pp., John Wiley, New York.

Hirth, G., and J. Tullis (1994), The brittle-plastic transition in experimentally deformed quartz aggregates, *J. Geophys. Res.*, *99*(B6), 11,731–11,747, doi:10.1029/93JB02873.

Hogenboom, D. L., J. S. Kargel, J. P. Ganasan, and L. Lee (1995), Magnesium sulfate-water to 400 MPa using a novel piezometer: Densities, phase equilibria, and planetelogical implications, *Icarus*, *115*, 258–277, doi:10.1006/icar.1995.1096.

Hooke, R. L., B. B. Dahlin, and M. T. Kauper (1972), Creep of ice containing dispersed fine sand, *J. Glaciol.*, *11*(63), 327–336.

Hyzak, J. M., and I. M. Bernstein (1976), The role of microstructure on the strength and toughness of fully pearlitic steels, *Metall. Trans. A*, *7*, 1217–1224, doi:10.1007/BF02656606.

Jacka, T. H. (1984), Laboratory studies on relationships between ice crystal size and flow rate, *Cold Reg. Sci. Technol.*, *10*, 31–42, doi:10.1016/0165-232X(84)90031-4.

Jaeger, J. C., and N. G. W. Cook (1979), *Fundamentals of Rock Mechanics*, 593 pp., Chapman and Hall, London.

Jones, S. J., and J. W. Glen (1969), The mechanical properties of single crystals of pure ice, *J. Glaciol.*, *52*, 463–473.

Jung, K., and H. Conrad (2001), Microstructure coarsening during static annealing of 60Sn40Pb solder joints: II Eutectic coarsening kinetics, *J. Electron. Mater.*, *30*(10), 1303–1307, doi:10.1007/s11664-001-0115-y.

Karato, S. I. (2008), *Deformation of Earth Materials: An Introduction to the Rheology of Solid Earth*, pp. 120–122, Cambridge Univ. Press, Cambridge, U. K.

Kirby, S. H. (1980), Tectonic stresses in the lithosphere: Constraints provided by the experimental deformation of rocks, *J. Geophys. Res.*, *85*, 6353–6363, doi:10.1029/JB085iB11p06353.

Kohlstedt, D. L., B. Evans, and S. J. Mackwell (1995), Strength of the lithosphere: Constraints imposed by laboratory experiments, *J. Geophys. Res.*, *100*(B9), 17,587–17,602, doi:10.1029/95JB01460.

Langford, G. (1977), Deformation of pearlite, *Metall. Trans. A*, *8*, 861–875, doi:10.1007/BF02661567.

Lee, S. M., and D. S. Stone (1994), Grain boundary sliding in as-cast Pb-Sn eutectic, *Scr. Metall. Mater.*, *30*(9), 1213–1218, doi:10.1016/0956-716X(94)90341-7.

Leith, A. C., and W. B. McKinnon (1996), Is there evidence for polar wander on Europa?, *Icarus*, *120*, 387–398, doi:10.1006/icar.1996.0058.

Li, X., D. Iliescu, and I. Baker (2009), On the effects of temperature on the strength of H$_2$SO$_4$-doped ice single crystals, *J. Glaciol.*, *55*(191), 481–484, doi:10.3189/002214309788816579.

Louchet, F. (2004), Ice: From dislocations to icy satellites, *C. R. Phys.*, *5*, 687–698, doi:10.1016/j.crhy.2004.09.001.

Luttrell, K., and D. Sandwell (2006), Strength of the lithosphere of the Galilean satellites, *Icarus*, *183*(1), 159–167, doi:10.1016/j.icarus.2006.01.015.

Mangold, N., P. Allemand, P. Duval, Y. Geraud, and P. Thomas (2002), Experimental and theoretical deformation of ice-rock mixtures: Implications on rheology and ice content of Martian permafrost, *Planet. Space Sci.*, *50*, 385–401, doi:10.1016/S0032-0633(02)00005-3.

McCarthy, C., R. F. Cooper, S. H. Kirby, K. D. Rieck, and L. A. Stern (2007a), Solidification and micostructures of binary ice-I/hydrate eutectic aggregates, *Am. Mineral.*, *92*, 1550–1560, doi:10.2138/am.2007.2435.

McCarthy, C., K. D. Rieck, S. H. Kirby, W. B. Durham, L. A. Stern, and R. F. Cooper (2007b), Crystal growth of ice-I/hydrate eutectic binary solutions, in *Physics and Chemistry of Ice*, edited by W. F. Kuhs, pp. 391–398, R. Soc. of Chem., Cambridge, U. K.

McCord, T. B., et al. (1998), Salts on Europa's surface detected by Galileo's near-infrared mapping spectrometer, *Science*, *280*, 1242–1245, doi:10.1126/science.280.5367.1242.

McCord, T. B., et al. (1999), Hydrated salt minerals on Europa's surface from the Galileo near-infrared mapping spectrometer (NIMS) investigation, *J. Geophys. Res.*, *104*, 11,827–11,851, doi:10.1029/1999JE900005.

McNutt, M. K. (1984), Lithospheric flexure and thermal anomalies, *J. Geophys. Res.*, *89*, 11,180–11,194, doi:10.1029/JB089iB13p11180.

Mei, Z., and J. W. Morris (1992), Characterization of eutectic Sn-Bi solder joints, *J. Electron. Mater.*, *21*(6), 599–607, doi:10.1007/BF02655427.

Murray, B. J., and A. K. Bertram (2008), Inhibition of solute crystallization in aqueous H$^+$–NH$_4$$^{4+}$–SO$_2^{4}$–H$_2$O droplets, *Phys. Chem. Chem. Phys.*, *10*(22), 3287–3301, doi:10.1039/b802216j.

Nakamura, T., and S. J. Jones (1970), Softening effect of dissolved hydrogen chloride in the crystals, *Scr. Metall.*, *4*, 123–126, doi:10.1016/0036-9748(70)90176-6.

Nakamura, T., and S. J. Jones (1973), Mechanical properties of impure ice crystals, in *Physics and Chemistry of Ice*, edited by E. Whalley, S. J. Jones, and L. W. Gold, pp. 365–369, R. Soc. of Can., Ottawa.

Paterson, W. S. B. (1991), Why ice-age ice is sometimes "soft", *Cold Reg. Sci. Technol.*, *20*, 75–98, doi:10.1016/0165-232X(91)90058-O.

Peterson, R. C., and R. Wang (2006), Crystal molds on Mars: Melting of a possible new mineral species to create Martian chaotic terrain, *Geology*, *34*, 957–960, doi:10.1130/G22678A.1.

Peterson, R. C., W. Nelson, B. Madu, and H. F. Shurvell (2007), Meridianiite: A new mineral species observed on Earth and predicted to exist on Mars, *Am. Mineral.*, *92*, 1756–1759, doi:10.2138/am.2007.2668.

Prockter, L. M., and R. T. Pappalardo (2000), Folds on Europa: Implications for crustal cycling and accommodation of extension, *Science*, *289*, 941–943, doi:10.1126/science.289.5481.941.

Raj, S. V. (2002), Power-law and exponential creep in class M materials: Discrepancies in experimental observations and implications for creep modeling, *Mater. Sci. Eng. A*, *322*, 132–147, doi:10.1016/S0921-5093(01)01126-1.

Scholz, C. H. (1988), The brittle-plastic transition and the depth of seismic faulting, *Geol. Rundsch.*, *77*(1), 319–328, doi:10.1007/BF01848693.

Senkov, O. N., and M. M. Myshlyaev (1986), Grain growth in a superplastic Zn-22% Al alloy, *Acta Metall.*, *34*(1), 97–106, doi:10.1016/0001-6160(86)90236-1.

Shi, X. Q., Z. P. Wang, W. Zhou, H. L. J. Pang, and Q. J. Yang (2002), A new creep constitutive model for eutectic solder alloy, *J. Electron. Packag.*, *124*, 85–90, doi:10.1115/1.1462624.

Shi, X. Q., Z. P. Wang, Q. J. Yang, and H. L. J. Pang (2003), Creep behavior and deformation mechanism map of Sn-Pb eutectic solder alloy, *J. Eng. Mater. Technol.*, *125*, 81–88, doi:10.1115/1.1525254.

Spaun, N. A., and J. W. Head III (2001), A model of Europa's crustal structure: Recent Galileo results and implications for an ocean, *J. Geophys. Res.*, *106*, 7567–7576, doi:10.1029/2000JE001270.

Turnbull, D. (1952), Kinetics of solidification of supercooled liquid mercury droplets, *J. Chem. Phys.*, *20*(3), 411–424, doi:10.1063/1.1700435.

Weertman, J. (1983), Creep deformation of ice, *Annu. Rev. Earth Planet. Sci.*, *11*, 215–240, doi:10.1146/annurev.ea.11.050183.001243.

Weertman, J., and J. R. Weertman (1975), High temperature creep of rock and mantle viscosity, *Annu. Rev. Earth Planet. Sci.*, *3*, 293–315, doi:10.1146/annurev.ea.03.050175.001453.

White, S. R. (2001), Textural and microstructural evidence for semi-brittle flow in natural fault rocks with varied mica contents, *Int. J. Earth Sci.*, *90*, 14–27, doi:10.1007/s005310000166.

Wood, G. R., and A. G. Walton (1970), Homogeneous nucleation kinetics of ice from water, *J. Appl. Phys.*, *41*, 3027–3036, doi:10.1063/1.1659359.

Zhan, C. (1993), Sea ice behaviour in creep/fracture regime: An experimental and theoretical study, Ph.D. thesis, Univ. of Ottawa, Ottawa.

Zoback, M. D., and J. Townend (2001), Implications of hydrostatic pore pressures and high crustal strength for the deformation of intraplate lithosphere, *Tectonophysics*, *336*, 19–30, doi:10.1016/S0040-1951(01)00091-9.

R. F. Cooper and D. L. Goldsby, Department of Geological Sciences, Brown University, Box 1846, Providence, RI 02912, USA. (reid_cooper@brown.edu; david_goldsby@brown.edu)

W. B. Durham, Department of Earth, Atmospheric and Planetary Sciences, Massachusetts Institute of Technology, 54-710, 77 Massachusetts Ave., Cambridge, MA 02139, USA. (wbdurham@mit.edu)

S. H. Kirby, U.S. Geological Survey, 345 Middlefield Rd., MS 977, Menlo Park, CA 94025, USA. (skirby@usgs.gov)

C. McCarthy, Earthquake Research Institute, University of Tokyo, 1-1-1 Yayoi, Bunkyo-ku, Tokyo 113-0032, Japan. (mccarthy@eri.u-tokyo.ac.jp)